Original Paper

Transmission-Based Muography for Ore Bodies Prospecting: A Case Study from a Skarn Complex in Italy

Tommaso Beni ,[1,9] **Diletta Borselli** ,[2,3,4] **Lorenzo Bonechi** ,[2] **Massimo Bongi** ,[2,4]
Debora Brocchini,[5] **Roberto Ciaranfi,**[2] **Luigi Cimmino** ,[6,7] **Vitaliano Ciulli** ,[2,4]
Raffaello D'Alessandro ,[2,4] **Andrea Dini** ,[8] **Catalin Frosin** ,[2,4] **Giovanni Gigli** ,[1]
Sandro Gonzi ,[2,4] **Silvia Guideri,**[5] **Luca Lombardi,**[1] **Massimiliano Nocentini** ,[1]
Giulio Saracino ,[6,7] **and Nicola Casagli** [1]

Transmission-based muography (TM) is an innovative imaging technique based on the measurement and analysis of the cosmic ray muons flux attenuation within the target under investigation. This technique allows imaging inner-body density differences and has successfully been applied in a wide range of research fields: geology, archaeology, engineering geology and civil engineering. The aim of this study is to show the reliability of TM as an innovative, noninvasive geophysical method for ore body prospecting and other mining related studies. The measurements were carried out at the Temperino mine in the San Silvestro Archaeological and Mining Park (Campiglia Marittima, Italy), where several magmatic and metasomatic geological units are embodied. Among them, a Cu–Fe–Zn–Pb(–Ag) sulfide skarn complex primarily composed by hedenbergite and ilvaite minerals. Using the acquired muon imaging data obtained with the MIMA (Muon Imaging for Mining and Archaeology) detector prototype (cubic detector of $0.5 \times 0.5 \times 0.5$ m^3), the presence of a high-density vein inside the skarn body within the rock volume above the muon detector was identified, localized and interpreted. Applying a back-projection algorithm to the obtained 2D transmission map made it possible to estimate and visualize as point cloud data, in a 2D or 3D environment, the identified high-density body and its relative distance from the detector. The results of this study highlight the potential of muography as a support tool to other geophysical methods in the field of mining exploration.

KEY WORDS: Muon radiography, Muography, Skarn ore body prospection, Mining exploration, Geophysical imaging.

[1]Department of Earth Sciences, University of Florence, Via Giorgio La Pira 4, 50121 Florence, Italy.

[2]Division of Florence, National Institute for Nuclear Physics INFN, Via Bruno Rossi 1, 50019 Sesto Fiorentino, Italy.

[3]Department of Physics and Geology, University of Perugia, Via Alessandro Pascoli, 06123 Perugia, Italy.

[4]Department of Physics and Astronomy, University of Florence, Via Giovanni Sansone 1, 50019 Sesto Fiorentino, Italy.

[5]Parchi Val Di Cornia S.P.A, Via Giovanni Lerario 90, 570254 Piombino, Italy.

[6]Department of Physics "Ettore Pancini", University of Naples Federico II, Via Cinthia 21, 80126 Naples, Italy.

[7]Division of Naples, National Institute for Nuclear Physics INFN, Via Cinthia, 80126 Naples, Italy.

[8]Institute of Geosciences and Georesources CNR, 56127 Pisa, Italy.

[9]To whom correspondence should be addressed; e-mail: tommaso.beni@unifi.it

INTRODUCTION

Muography and Applications

Muon radiography also known as muography is a noninvasive and passive imaging technique that, by measuring the natural muon flux, can provide information on the internal structures of a target (from metric to kilometric scale) under study. The muon ($\mu^{\pm}$) is an elementary particle with characteristics similar to the electron but with a mass 200 times larger. Muography exploits atmospheric muons that hit the Earth's surface at a rate of about 100 Hz/m^2 at European latitudes (Bonechi et al., 2020a, 2020b; Zyla et al., 2020). Muons are naturally produced in the upper layers of the Earth's atmosphere ($\sim$15–17 km above sea level) by the interactions between high-energy primary cosmic rays, i.e., particles and atomic nuclei coming from outside the planet, and atmospheric nuclei such as nitrogen and oxygen. Subnuclear particles produced by these collisions, mainly pions and kaons, then decay into muons (Olive, 2016; Zyla et al., 2020). Muons are unstable particles with average lifetime $\tau \approx 2.2$ µs (Zyla et al., 2020). Such high lifetime allows high-energy muons to reach the Earth's surface and cross hundreds of meters of rocks. Thus, they are suitable for imaging because they are highly penetrating particles characterized by low interactions with matter, which follow relatively straight line trajectories (Bryman et al., 2014). Muography measures the average density along various directions, or line of sight (LoS), usually identified by two angles: the zenith angle (θ) and the azimuth angle (φ).

The angular distribution of the atmospheric muons flux is proportional to $\cos^n\theta$ (Lin et al., 2010; Zyla et al., 2020), where n is a parameter dependent on the particle energy and the location on the Earth's surface. Generally, the ground level overall muon angular distribution is proportional to $\cos^2\theta$ (Grieder, 2001; Lin et al., 2010).

Muography comes in two flavors: transmission-based muography (TM) also known as transmission muography and scattering-based muography (SM). The former was employed in this study, as it is generally used to study large and extended targets such as mountains, volcanoes, or mine sites (Schouten & Ledru, 2018; Saracino et al., 2019; Schouten, 2019), while the latter is usually employed to image smaller sized targets such as nuclear waste casks or lorry containers (Mahon et al., 2019; Vanini et al., 2019).

One of the first applications of muon radiography was in 1955, where ice thickness above a tunnel (Edward Pelham, 1955) was measured. Since then, the TM has been applied in a wide range of research fields. The first archaeological application was in the 1960s, when Alvarez et al. (1970) excluded the existence of hidden chambers in the Chephren Pyramid in Egypt. In 1979, a simulated study tested the reliability of muon radiography for mining exploration evaluating in situ rock density (Malmqvist et al., 1979). These pioneering applications triggered a worldwide spread of muography. In the last 20 years, particular attention was given to volcanology applications in Italy (Carbone et al., 2014; Tioukov et al., 2017; Bonechi et al., 2018; D'Alessandro et al., 2019; Tioukov et al., 2019), in Japan (Tanaka et al., 2007, 2014; Tanaka, 2016) and in France (Lesparre et al., 2012; Jourde et al., 2016). There were also archaeological studies (Menichelli et al., 2007; Saracino et al., 2019), mining deposits exploration, rock density measurements (Bryman et al., 2014; Tanaka, 2015; Guardincerri et al., 2017; Schouten, 2019) and civil and environmental engineering investigations (Baccani et al., 2021). Interested readers are referred to the many excellent reviews of the literature (Saracino & Cârloganu, 2012; Tanaka, 2017; Procureur, 2018; Kaiser, 2019; Tanaka & Oláh, 2019; Bonechi et al., 2020a, 2020b).

In the last four years, seven measurement campaigns were carried out by our group at the Temperino Mine in the San Silvestro Archaeological and Mining Park (Campiglia Marittima, Italy) using the MIMA (Muon Imaging for Mining and Archaeology; Fig. 1) muon detector. Among the campaign results were the finding of previously unknown chambers and the observation of high-density plumes within the mine body (Borselli, 2018; Baccani et al., 2019; Bonechi et al., 2020a, 2020b).

The apparatus used for the measurements was the MIMA detector, a small and rugged prototype ($0.5 \times 0.5 \times 0.5$ m^3) muon tracker developed by physicists of the National Institute for Nuclear Physics (INFN) and the Department of Physics and Astronomy of Florence (Fig. 1b) (Baccani et al., 2018). The front-end electronics and DAQ of the MIMA detector was implemented thanks to the knowledge and expertise acquired on the MURAVES experiment (MUon RAdiography of VESuvius) (Cimmino et al., 2017; Bonechi et al., 2018). The aim of the MIMA project is to investigate muon imaging techniques, applied to mining, archaeology, civil engineering, and engineering geology issues
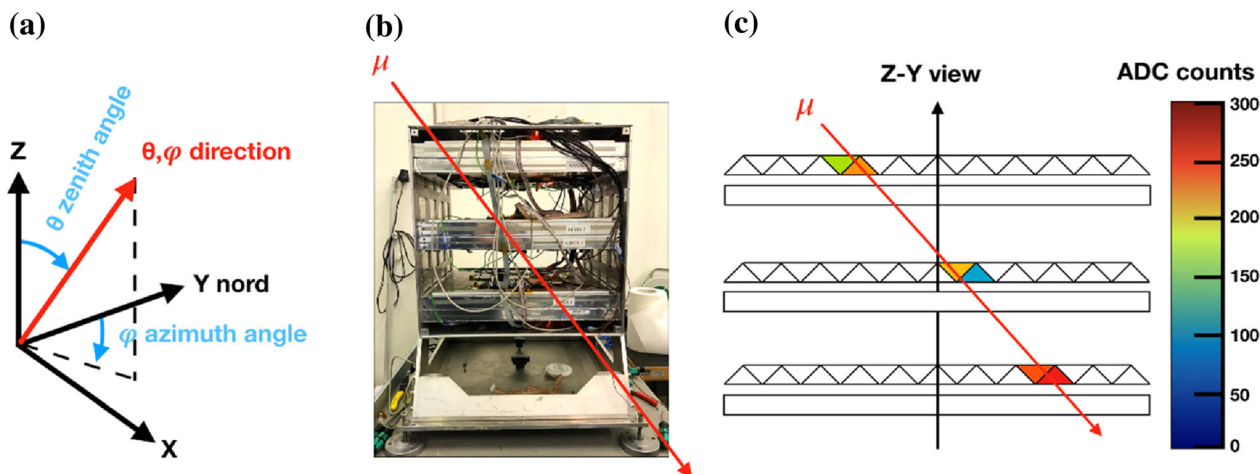
(a) **(b)** **(c)**

Figure 1. Characteristics of the MIMA detector: (**a**) coordinate system with zenith and azimuth angles; (**b**) cubic structure of the detector ($0.5 \times 0.5 \times 0.5$ m^3) consisting of three modules composed by two orthogonal tracking plane X–Y; (**c**) section showing the 21 plastic scintillator bars inside each X planes and an example of a track reconstruction process in Z-Y view. The color scale values represent the range of intensity detected on the single bars crossed by a muon. ADC counts are the analog-to-digital converted values.

(e.g., identification of cavities or volumes with density anomalies. The present study validates and confirms the reliability of TM, using the MIMA detector, both for mining exploration purposes and also for preliminary ore bodies prospection in Cu–Fe–Pb–Zn(–Ag) skarn ore deposits. This study shows how muographic surveys could become a complementary tool to other traditional geophysical methods (Bryman et al., 2014; Zhang et al., 2020; Okada, 2021) like gravimetric, seismic and magnetic surveys; a detailed review of this subject is made by Okada (2021).

Geological and Structural Setting of the Area of Campiglia Marittima

The area of Campiglia Marittima is characterized by lithologies belonging to the Tuscan Units, Ligurian Units and the more recent magmatic and hydrothermal units (Fig. 2). The municipality of Campiglia extends above a horst structure with N–S-orientated Mesozoic carbonate rocks belonging to the Tuscan Nappe, surrounded by a Jurassic ophiolitic-flysch sequence of the Ligurian Units (Dini et al., 2005; Vezzoni et al., 2018). The carbonate succession consists of Rhaetian platform carbonates (Calcari a Rhaetavicula Contorta Formation), Jurassic massive limestone (Calcare Massiccio Formation) and red nodular limestone with ammonites

(Rosso Ammonitico Formation) (Vezzoni et al., 2018).

The Miocene–Quaternary extensional tectonics of the inner part of the Northern Apennine (orogenic chain with thrust and folds) led to the formation of a high-angle NW–SE normal fault system and to crustal anatectic and mantle-derived magmatism products (Acocella et al., 2000).

In Campiglia Marittima, the Mesozoic sedimentary carbonate succession was intruded by a granitic pluton around 5.7 Ma, which nowadays crop out at Botro ai Marmi (Borsi et al., 1967). Following this magmatic and metasomatic event, which formed the primary skarn bodies of the area around 4–5 Ma, new intrusions of subvolcanic igneous rocks took place (Borsi et al., 1967; Da Mommio et al., 2010; Vezzoni et al., 2016; Paoli et al., 2019).

Felsic and mafic porphyritic dikes crosscut the older contacts and host rocks, forming ore deposits of Cu–Fe–Pb–Zn(–Ag) in contact surfaces with the skarn bodies (Figs. 2, 3). Thus, the magmatic and hydrothermal succession of events can be summarized by the following stages (Da Mommio et al., 2010; Vezzoni et al., 2016): (1) emplacement of the Botro ai Marmi monzogranite pluton, which created an extended contact-metamorphic aureole (marble host rocks; MAS) and triggered the metasomatic processes that created several skarn bodies (SKA) with no symmetrical mineralogical zoning; (2) intrusion of mafic porphyry dikes (PM) in the
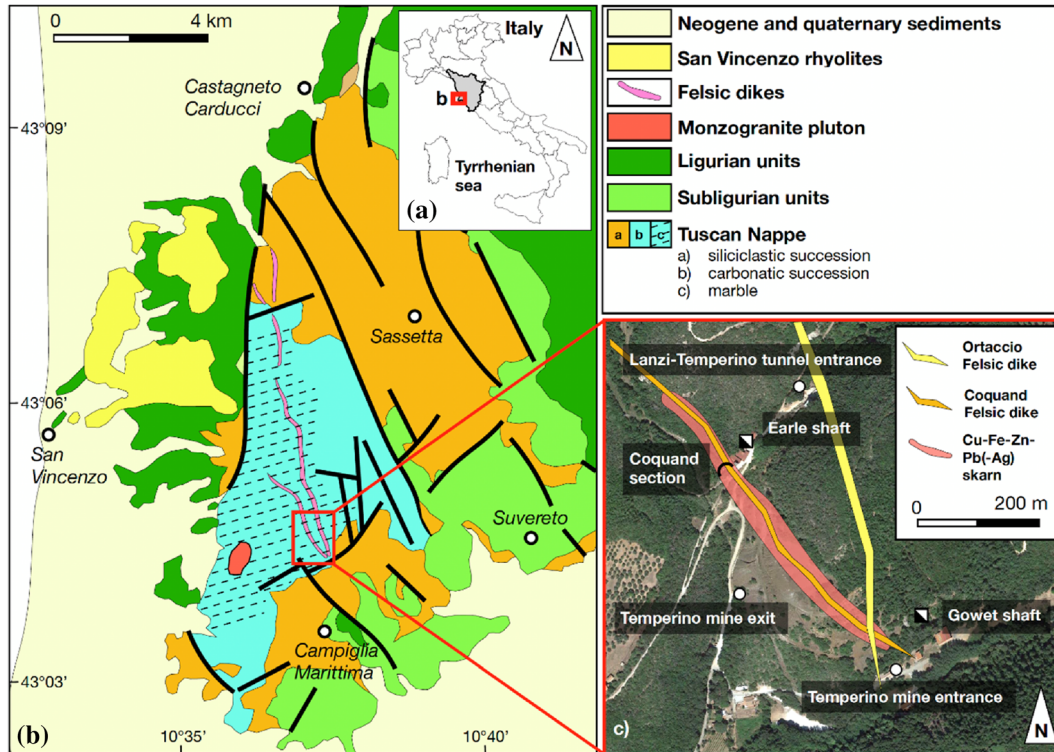
Figure 2. Case study location: (**a**) the area of Campiglia Marittima (Italy); (**b**) schematic geological map of the study area modified from (Da Mommio et al., 2010) and (Vezzoni et al., 2018); (**c**) satellite image with interpretative land-drawing of the skarn body of the Temperino mine and the emplaced felsic dikes.

Temperino mining area, which are associated with the skarn bodies and never directly intruding the MAS; (3) intrusion of felsic (acid) porphyry (Coquand felsic dike PFC and Ortaccio felsic dike PFO), which cross all previous contacts and lithologies, forming epidosite in contact with the skarn.

Skarn Deposits and Magmatic Units

The area of Campiglia Marittima is a well-known case study for skarn-related mineralization linked to magmatic events. Since Etruscan times till the end of the twentieth century, a location where Cu, Fe, Pb, Zn, Ag were mined was located (Sciarra et al., 2015; Vezzoni et al., 2016). Over the years, several scientists proposed many models to describe the outcropping rocks and to understand mineralogical zonation spatial relationships and genesis of the metasomatic rocks (Da Mommio et al., 2010; Vezzoni, 2014). In the last decade, a new conceptual model was proposed by Vezzoni et al. (2016)

describing the skarn body as a deposit with no-symmetrical mineralogical zone with respect to the central axis of the skarn itself, which could be an example of distal Zn–Pb(–Ag) skarn characterized by a reverse telescoping process.

The Campiglia Marittima is characterized by the presence of several distal skarn deposits, hosted in marble, and outcropping on at least 10 km^2. Among them, the most common are: Zn–Pb(–Ag) skarn body in the Lanzi Mine area and two peculiar Cu–Fe–Zn–Pb(–Ag) skarn bodies in the Temperino mine area (Fig. 3). The skarn bodies are primarily composed of monomineralic massive and rhythmically layered ilvaite and fibrous-radiating hedenbergite facies. Based on relative abundances of the latter, Vezzoni et al. (2016) identified three skarn facies: (1) rhythmically layered hedenbergite-ilvaite; (2) fibrous-radiating hedenbergite; (3) massive ilvaite.

Typical densities of the lithologies and minerals present at the Temperino mine are reported in Table 1. Due to the variability of the % by weight values of each mineral inside the considered thick-

ness of rocks, it is often possible to obtain different density values for the same lithology within the skarn body, thus giving rise to possible uncertainties in the TM interpretation. Ore bodies are dominated by sphalerite, galena, chalcopyrite, pyrrhotite, pyrite and magnetite (see density values in Table 1).

The mafic porphyry intrusions are irregularly distributed as subvertical dikelets and as infilling of the primary skarn cavities for about 10% of the Earle skarn total volume (Fig. 3). Instead, the felsic porphyry intrusions span entirely across the central

Table 1. Typical density values $\rho_{average}$ for lithologies and minerals assemblage present at the Temperino mine, data from Temperino mine and literature (Yang et al., 2013; Baccani et al., 2019)

Lithology and minerals	$\rho_{average}$(g/cm^3)
Marble	2.4–2.7
Felsic Porphyry	2.5–2.8
Mafic Porphyry	2.6–3.0
Skarn hedenbergite + ilvaite	3.3–3.5
Skarn with Cu-Fe sulfides (associated with mafic porphyry intrusion)	3.5–3.7
Massive hedenbergite	∼3.6
Massive ilvaite	∼4.0
Chalcopyrite	∼4.0
Pyrrhotite	4.1–4.2
Pyrite	4.8–5.0
Magnetite	5.0–5.2

zone of main skarn body with similar spatial orientation (Fig. 2c). A peculiar feature of the Campiglia skarns is the primary macroporosity (presence of voids in 2–15% of the skarn total volume) that allowed the intrusion of the mafic porphyry and the deposition of sulfide ores (Dini et al., 2013; Vezzoni et al., 2016).

Case Study: Temperino Mine

The Temperino mine area had a long history of mining activity since the Etruscan–Roman times (seventh to first century BC) until the end of the twentieth century (Brocchini et al., 2017). Different mining techniques were used during the three main exploitation periods: narrow vertical shafts dug from the surface following the ores underground (Etruscan and Middle Age period), opencast mines often cutting across the mine works of the previous period (sixteenth century period), and horizontal galleries excavated in the Cu-Fe rich ore bodies (modern period) (Fig. 3). During the last period, the mine produced 12,000 tons of galena (average Ag content of 0.1%), 26,000 tons of sphalerite (average Zn content of 54%) and 30,000 tons of chalcopyrite (average Cu content of 24%). In 1983, the last mining permit expired and the whole mining area (Temperino–Lanzi–Ortaccio–Manienti) became
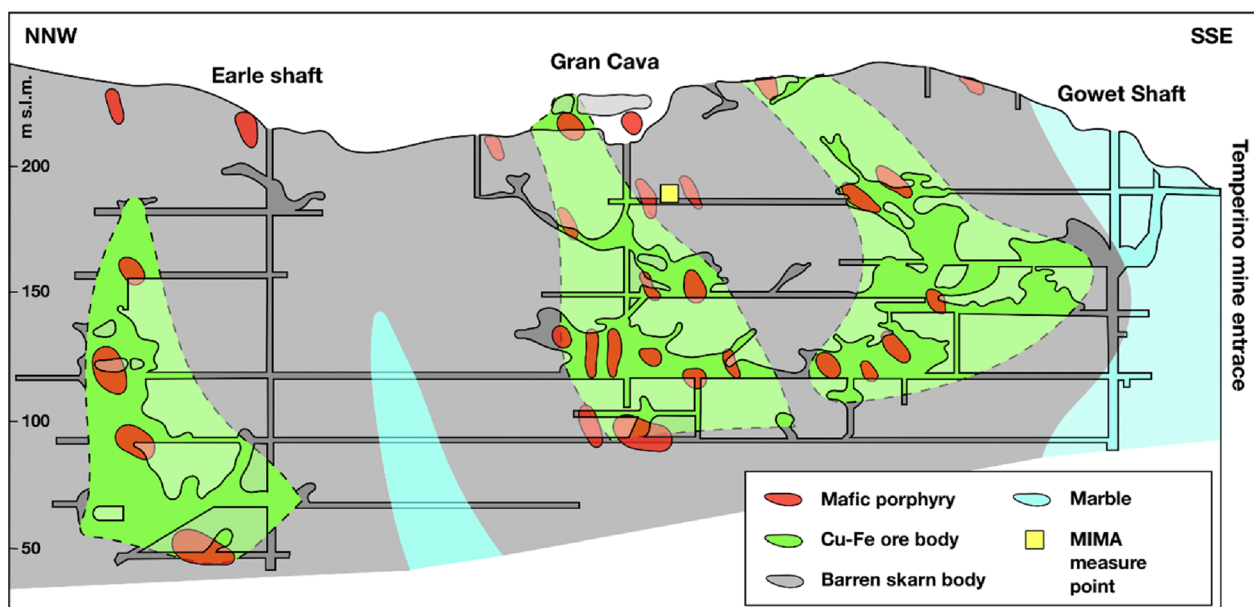

Figure 3. Geological section NNW-SSE of the outcropping Cu-Fe-Zn-Pb(-Ag) skarn bodies in the Temperino mine area between the Earle shaft and Le Marchand shaft (modified after (Vezzoni et al., 2016)). The yellow square indicates the measure point of MIMA detector inside the touristic tunnel.

part of the San Silvestro Archaeological and Mining Park (Da Mommio et al., 2010; Sciarra et al., 2015). The importance given to this mining area for more than 2,000 years is due to the presence of the skarn bodies.

Skarn ore deposits are one of the major sources of Cu, Pb, Zn, Ag and Au on Earth. For this reason, mining exploration of skarn complexes and systems plays an important role in scientific and industrial research (Meinert et al., 2005; Tinagli et al., 2021). The Temperino mine levels and galleries were carved, vertically and horizontally, within the Campiglia's skarn bodies searching for Cu–Fe rich ore deposits (Fig. 3). Among them, the main Cu–Fe ore deposits are hosted within the skarn body, while but rarely the skarn–marble contact surfaces are mineralized. In the Temperino and Lanzi mines, three different ore types were mined: (1) Zn–Pb(–Ag) type (sphalerite, galena, pyrite); (2) Cu–Fe type (chalcopyrite, pyrrhotite, pyrite, magnetite); and (3) Zn–Pb–Cu(–Ag) type. The Zn–Pb(–Ag) type, exploited at the Lanzi mine, is not associated with mafic rocks; the Cu–Fe type is strictly associated with the intruded mafic porphyry masses (and plays a key role in the interpretation process of the presented study), and the Zn–Pb(–Ag) type only occurs associated with the Cu–Fe type ore and the mafic porphyry dikes (only at the Temperino mine). Focusing on the Cu–Fe type, it is represented by massive chalcopyrite–pyrrhotite–pyrite (density in Table 1) and can contain up to 10% by weight of Cu in decametric narrow bands between skarn and mafic intrusion (Vezzoni et al., 2016). Cu–Fe ores can reach 4–5% by weight in vein systems extended inside the skarn for meters to ten of meters. The Cu–Fe ores are spatially associated with mafic intrusions, whose shapes and locations depend on the primary skarn macroporosity mainly present in the internal portions of the skarn (Fig. 3). The average percentage of Cu in Cu–Fe ore type was in the range of 1.9–2.7% by weight.

MATERIAL AND METHODS

The MIMA detector was used in 2019–2021 to measure the underground muon flux along the tunnel used for tourist visits at the Temperino mine. Overall, seven measurements were carried out, but only the measured point shown in Figure 4 was used for this study. Detailed field surveys and reviews of the previous geological surveys and studies were performed. Detailed terrestrial laser scanner (TLS) surveys were carried out inside and outside the mine to obtain a georeferenced three-dimensional (3D) model of the first level of the mine tunnels and of the Gran Cava cavity (a big known cavity). The TLS output data consist of a georeferenced point cloud composed of tens of millions of points. Then, the TLS data were merged with a 1×1 m resolution digital terrain model (DTM) of the area (Regione Toscana, 2022) to perform the muon flux simulations used for image reconstruction. This georeferenced 3D model was used to define the coordinates of the MIMA detector inside the gallery with decimetric accuracy (Fig. 4a): X = 631,494.21, Y = 477,044.10, Z = 184.90 in the EPSG:32,632 WGS 84 / UTM zone 32N reference coordinate system.

MIMA Detector and Tracks Reconstruction

The MIMA detector (or tracker) was designed for mining and archaeological applications, and its main characteristics are its small size ($0.5 \times 0.5 \times 0.5$ m^3), low weight ($\sim$50 kg), low power consumption ($\sim$30 W) and angular resolution (σ_θ) of about 7 mrad. Thus, in principle, it enables to distinguish, at a distance of 50 m, objects about 30 cm apart. MIMA is made up of three modules composed of two orthogonal tracking planes (X–Y) each composed of 21 plastic scintillator bars (Fig. 1b, c). Each module has a 40×40 cm^2 active detection surface, and all six planes are identical and independent. These three modules are inserted in a cubic aluminum box mounted on an altazimuthal platform so that the detector can be pointed at the object of interest.

Further details on the construction of the MIMA detector are reported in (Baccani et al., 2018; Bonechi et al., 2018; Baccani et al., 2019). The X–Y coordinate points—one per module—allow to reconstruct the passing muon trajectory in three dimensions. Only single muon event tracks are selected and, to increase the detector acceptance to approximately $\pm$ 60°, muons passing through only two modules are also accepted. The detector structure and an example of track reconstruction are shown in Figure 1.

Transmission-based Muography Imaging Data

The TM technique used for this study relies on an accurate track reconstruction of the muon events arriving from various LoS (Fig. 5a, b) within the
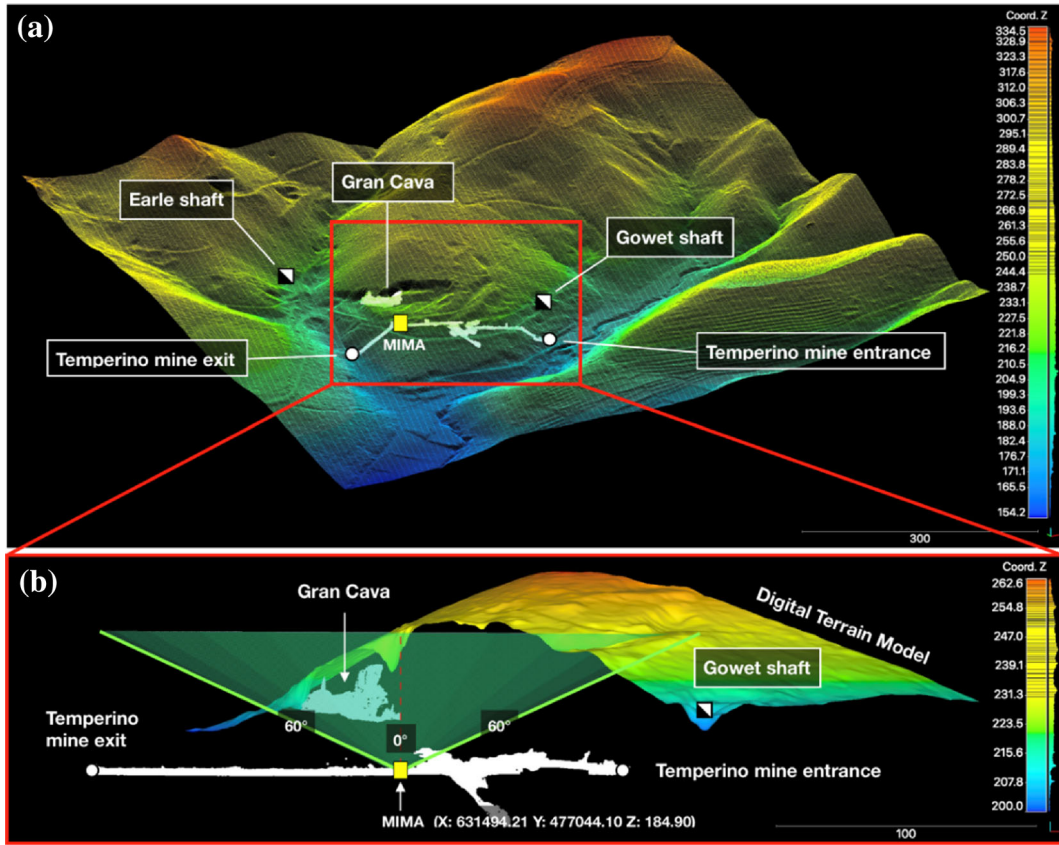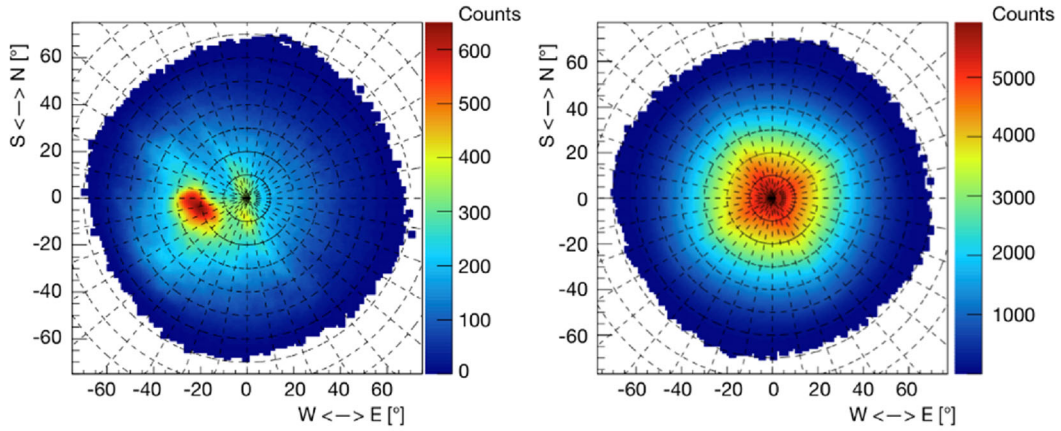
Figure 4. Spatial location of the Temperino mine tunnel in the study area and 3D data: (**a**) surface and mine point clouds, data from the DTM and the TLS survey, the yellow square indicates the MIMA detector measure point inside the first level of the mine and the color scale represents the meters above sea level; (**b**) E–W section showing the acceptance cone of the MIMA detector, the Gran Cava cavity falls within the cone.

muon detector acceptance (about $\pm 60°$; Fig. 4b). This technique is mainly based on two configuration measurements: target and free-sky. The former refers to the muon flux measurement carried out inside the mine, where rock strata between the detector and the surface constitute the target, while the latter refers to the muon flux measurements carried out outside the mine, without any target interposed between the detector and the sky (free-sky), keeping the same orientation of the target one. In addition to these field measurements, simulations of the underground muon flux measurement were done using the detector center and the surface DTM to evaluate the expected transmission values for different rock density values. These simulations are based on a custom code that relies on DTM and muon transmission tables obtained from various sources (Bonechi et al., 2005; Zyla et al., 2020). Several simulations were performed considering the rock

between the detector (considered as a point-like detector) and the surface as a homogeneous material. These types of simulations consider only the loss of energy in a material of a certain assigned density and do not consider the details of muon-matter interactions. This could cause a non-negligible bias for rock thickness greater than 300 m (Lechmann et al., 2018), but not in our study at the Temperino mine, where MIMA was placed at about 50 m depth.

The measured muon transmission (T_m) depends on the observation direction (Fig. 5c), identified by the zenith angle (θ), which is the angle between the vertical direction and the LoS, and the azimuth angle (φ), which is the clockwise angle from North direction; and T_m is defined as:

$$T_m = \frac{\phi_{m,target}(\theta, \varphi)}{\phi_{m,free-sky}(\theta, \varphi)} \qquad (1)$$

(a) Target configuration events $N_{target}(\theta, \varphi)$

(b) Free-sky configuration events $N_{free-sky}(\theta, \varphi)$

(c) Measured transmission $T_m(\theta, \varphi)$

(d) Simulated transmission $T_s(\theta, \varphi, \bar{\rho})$

(e) Relative transmission $T_{rel}(\theta, \varphi, \bar{\rho})$

(f) Average density $\bar{\rho}(\theta, \varphi)$

◄**Figure 5.** TM data plotted in polar reference frame maps. The center is the vertical direction from the center of MIMA detector, the dotted circles correspond to direction with same zenith angle θ and the radial dotted lines indicate azimuth directions φ, both angles are represented with a 10° step: (**a**) track angular distribution for the target configuration; (**b**) track angular distribution for the free-sky configuration; (**c**) measured transmission inside the Temperino mine; (**d**) example of simulated transmission assuming an uniform density $\overline{\rho}(\theta, \varphi) =$ 3.2 g/cm³, this is just an arbitrary value that falls within the density range of skarn hedenbergite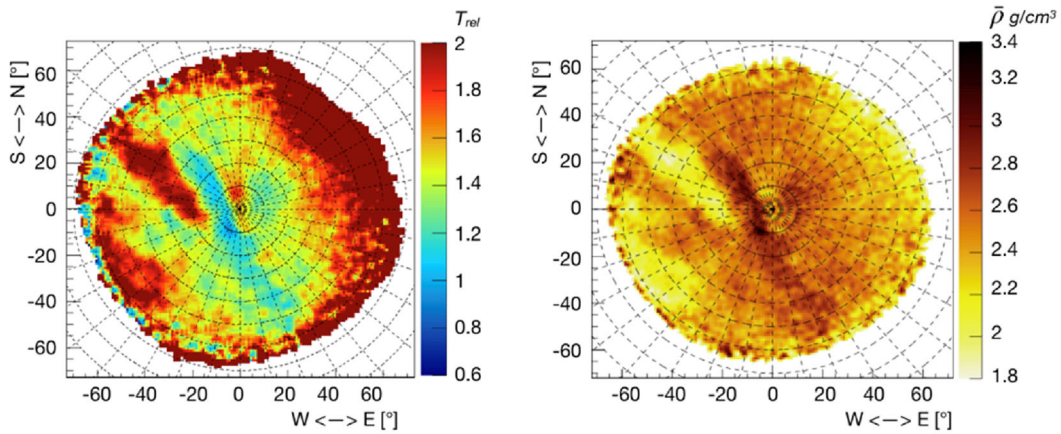/ilvaite and mafic porphyry (see Table 1); (**e**) relative transmission polar map for $\overline{\rho}(\theta, \varphi) =$ 3.2 g/cm³; (f) reconstructed average density distribution.

where $\phi_{m,target}$ is the muon flux measured by the MIMA tracker inside the mine gallery (Fig. 5a) and $\phi_{m,free-sky}$ is the muon flux measured in the free-sky configuration (outside the mine with the same underground orientation; Fig. 5b). The measured flux is defined as (Baccani et al., 2019):

$$\phi_m(\theta, \varphi) = \frac{N(\theta, \varphi)}{t A_{eff}(\theta, \varphi)} \qquad (2)$$

where $N(\theta, \varphi)$ is the number of tracks with (θ, φ) direction, t is the acquisition time and $A_{eff}(\theta, \varphi)$ is the effective area of the detector.

For the two measurement configurations (target and free-sky), the acceptance surface is identical, and trigger efficiency variations are negligible for this study. Thus, $A_{eff}(\theta, \varphi)$ is constant and the measured transmission equation can be simplified as:

$$T_m(\theta, \varphi) = \frac{N_{target}(\theta, \varphi)}{N_{free-sky}(\theta, \varphi)} \cdot \frac{t_{free-sky}}{t_{target}} \qquad (3)$$

The $T_m(\theta, \varphi)$ values can then be compared to the ones obtained from the simulations (Fig. 5c, d). The simulation was performed using the DTM of the area and the TLS survey data of the underground gallery. This additional 3D information allows to calculate rock thickness along the detector LoS (Fig. 4). Defining $L(\theta, \varphi)$ the distance between the center of MIMA and the terrain surface, assuming no cavities or anomalies in the matter traversed by the particles, the opacity X is defined as:

$$X(\theta, \varphi, \overline{\rho}) = \int_{LoS} \rho dL = \overline{\rho}(\theta, \varphi) \cdot L(\theta, \varphi) \qquad (4)$$

where ρ is the traversed matter density and $\overline{\rho}(\theta, \varphi)$ is the average density along the LoS. Thus, even a single TM measurement can in principle provide information about the traversed overburden matter.

Often it is not possible to carry out more than one TM measurement for several reasons: data acquisition time (could be several weeks), mining planning problems and/or underground logistic problems. In this study, only one measurement site dataset was analyzed to confirm how useful even a single TM measurement could be for mining activities. The simulated transmission $T_s(\theta, \varphi, \overline{\rho})$ is defined in the same manner as $T_m(\theta, \varphi)$ but with simulated muon fluxes for both free-sky and target configurations (Fig. 5d). The simulated muon fluxes are defined as:

$$\phi_{s,target}(\theta, \varphi, \overline{\rho}) = \int_{E_{min}(X)}^{\infty} j(\theta, \varphi, E) dE \qquad (5)$$

$$\phi_{s,free-sky}(\theta, \varphi) = \int_{E_0}^{\infty} j(\theta, \varphi, E) \qquad (6)$$

where $j(\theta, \varphi, E)$ is the differential muon flux as a function of muon trajectories (θ, φ) and muon energy (E). The lower integral limit $E_{min}(X)$, obtained from the opacity (X) exploiting the tabulated values available in the literature (Groom et al., 2001), is the minimum energy that a muon must have to be detected by MIMA in the target configuration (about 23 GeV considering an overlying standard rock with a density of 2.7 g/cm³ (Borselli, 2018)). The lower integral limit E_0 is equal to $E_{min}(X)$, but for the free-sky configuration, taking into account the opacity of the detector itself, the energy needed by a muon to cross the detector is about 130 MeV. For the differential muon flux, the values measured by the ADAMO experiment were used (Bonechi et al., 2005; Borselli, 2018; Baccani et al., 2019). Two main reasons justify the employment of these data: (1) ADAMO measurements were carried out at a similar latitude of the Temperino mine application (in Tuscany, respectively, in the municipality of Florence the former and municipality of Livorno the latter) at a roughly similar height above sea level; and (2) several published works have successfully relied on the ADAMO measurements (Bonechi et al., 2005; Baccani et al., 2019, 2021; Bonomi et al., 2022; Gonzi et al., 2022).

The simulated transmission (T_s) values depend on the constant average density assigned to the rock above the detector. For this study, several simulations were carried out using different density values ranging from 0.5 to 7 g/cm³. For each chosen density, the simulated transmission was compared to the measured one, obtaining the density profile values along the LoS in the target configuration.
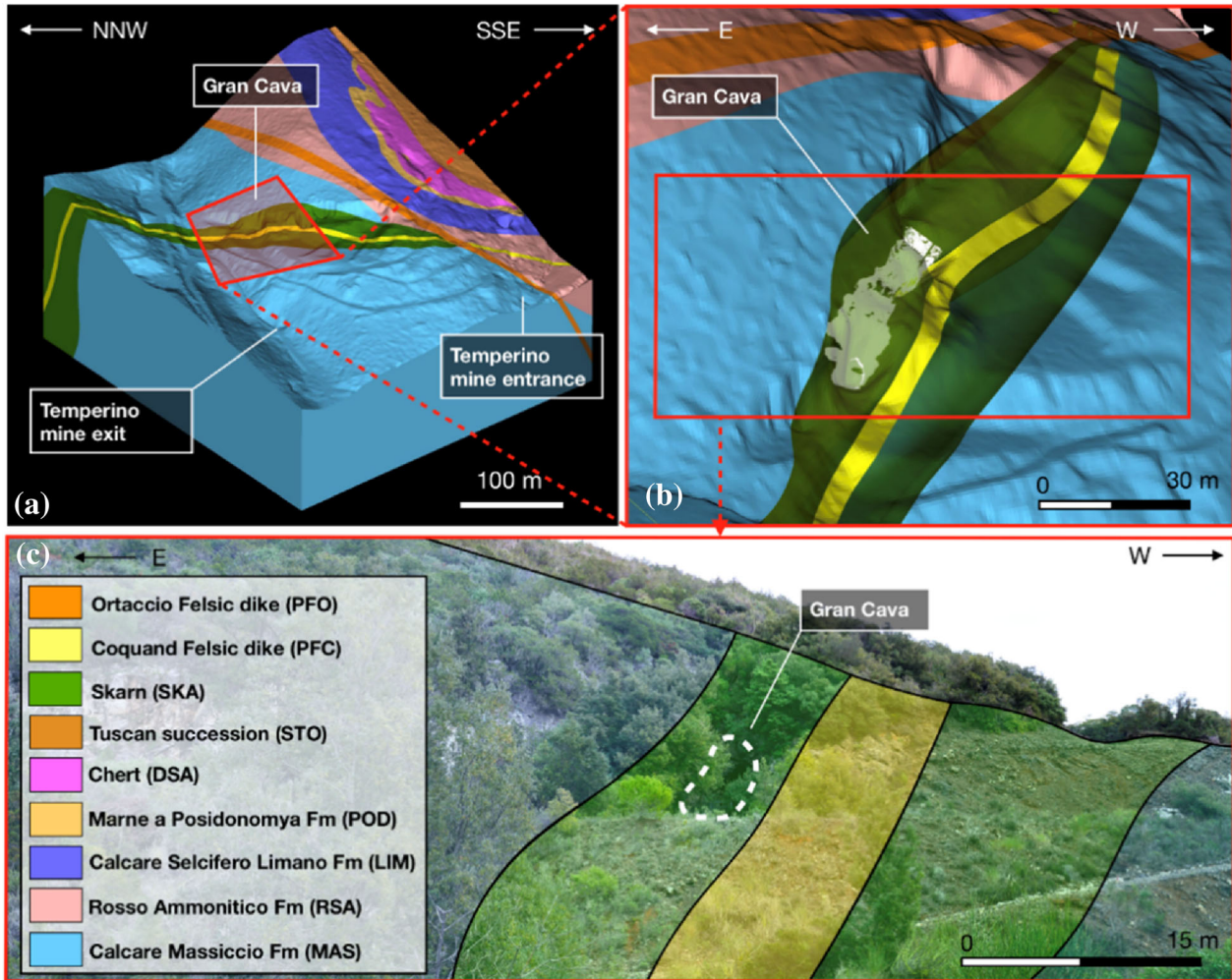
Figure 6. Geological model of the Temperino mine area: (**a**) 3D model of the area under study; (**b**) focus on the geological setting of the skarn body and felsic dike near to the Gran Cava; (**c**) land-drawing of the lithology outcropping on the hill area overlying the underground measurement.

The presence of high-density bodies is highlighted by a deficit in the $T_m(\theta, \varphi)$ relative to the simulated one, $T_s(\theta, \varphi, \overline{\rho})$, and it is visible in the relative transmission, T_{rel}, polar map (Fig. 5e). The latter is defined as:

$$T_{rel}(\theta, \varphi, \overline{\rho}) = \frac{T_m(\theta, \varphi)}{T_s(\theta, \varphi, \overline{\rho})} \quad (7)$$

It follows that, for bins in the polar map where the value of T_{rel} is near unity, the assigned density of $T_s(\theta, \varphi, \overline{\rho})$ along the relative LoS must correspond to the actual measured one. To ensure that the relative transmission is not affected by the acceptance of the detector, it is necessary to avoid any possible misalignment between the measured configuration

(target) and the simulated one. Therefore, a laser scanner survey was used to precisely locate the detector inside the mine. The position (orientation) of the detector extracted from the laser scanner has a centimetric uncertainty which can result in a up to 10–15 mrad (about 0.5–1°) uncertainty on the orientation of MIMA. Given the aim of this study, namely the investigation of targets of tens of meters at a reduced distance from the detector, this precision was more than enough.

From the comparison between the polar maps of T_m and T_s (Fig. 5c, d), one can easily discern high- and low-density regions with respect to the average simulated values. The results of this analysis are the 2D transmission maps and the 2D average

density polar maps shown in Figure 5e and f. Using custom algorithms, an estimate of the relative distances between the high-density region bins in the 2D density polar map and the MIMA detector was derived, and a 3D cloud of points corresponding to the anomalous density regions (Borselli, 2018) was obtained. To this end, a back-projection algorithm (Bonechi et al., 2015, 2019; Borselli et al., 2022) for muon imaging was applied to the single TM measurement taken in the mine. In particular, the back-projection method made it possible to estimate the 3D profile of the dense body "floor", one point for each bin of the polar map. The thickness/height of the dense body was estimated by combining the information obtained with the density map and information on the thickness of the material along the LoS crossing the dense body. In this way, two 3D point clouds were created: one representing the "floor" of the dense body and the other the "ceiling". Using these point clouds, it is possible to reconstruct a mesh of the high-density body profile, thus obtaining a 3D shape of the ore body using only the TM data from one site. The collected in situ geological information and the created 3D geological model were then used to validate the extent and shape and to infer the possible genesis of this reconstructed high-density body.

3D Data and Field Surveys

In the TM workflow, an important role is played by the underground and surface 3D surveys. In fact, the most reliable transmission simulations rely on an accurate and georeferenced DTM of the overlying hill and a 3D model of the mine gallery. In 2019, a detailed TLS survey was carried out at the Temperino mine (Baccani et al., 2019) and all the accessible and known cavities were mapped (the first level of the mine and the Gran Cava cavity). A point cloud of more than 50 M points was obtained, and it was utilized to compute rock thickness values between the MIMA detector underground and the overlying terrain surface. The more accurate are the point clouds/meshes employed for the simulations, the more reliable are the outputs of the muographic data analysis. Figure 4 shows the 3D environment created by merging the DTM and the TLS point clouds, with the position of MIMA and its acceptance. A review of most past studies in the Temperino mine area (Da Mommio et al., 2010; Dini et al., 2013; Vezzoni, 2014; Vezzoni et al., 2016, 2018;

Tinagli et al., 2021) was also performed to obtain fundamental geologic underground data of deeper galleries that are not anymore accessible. Moreover, a field survey was carried out inside the accessible tunnels in the Temperino mine and on the overlying hill, from the Earle shaft to Gowet shaft area, with the aim of understanding the chronological and spatial relationships among lithologies (host marble, skarn, mafic porphyry, and acid porphyry) and to collect outcrop photographs and rock samples. Therefore, it was possible to create a 3D geological map and a georeferenced 3D geological model of the Temperino mining area (Fig. 6), which constitutes a useful and detailed reference frame for the display, validation and interpretation of the TM data.

The 3D geological model created for this study (more details in the following section) was generated using Leapfrog Geo Seequent software through implicit 3D geological modeling (Copyright© Seequent Systems, Incorporated) (Seequent Software, 2022). This geological model relies on the available underground geological surveys data carried out by the last mining companies in the last half of the twentieth century. Nowadays, these surveyed mine levels are closed for safety issues. Because of this, the interpretation of the old data during the modeling process became important given the absence of a direct geognostic campaign survey. A reliable quantification of the possible systemic failures affecting the created geological model is not always possible. However, in this case, the rock mass within the detector acceptance, where the studied target was located, was easily accessible through the Gran Cava cavity and so it was possible to have a direct confirmation of the presence and the extent of the snake-shape body imaged with the TM data.

RESULTS

3D Data Interpretation and Visualization

For this study, the data acquired by the MIMA detector at the measurement point shown in Figure 4 were analyzed. The tracker was placed inside the tourist tunnel of the Temperino mine, about 50 m below the surface (184.9 m above sea level) and acquired about 1×10^6 events in 67 days. The results of the muon imaging method are reported in Figure 5. The obtained average density values $\overline{\rho}(\theta, \varphi)$ ranged from 1.8 up to 3.4 g/cm^3 (see average
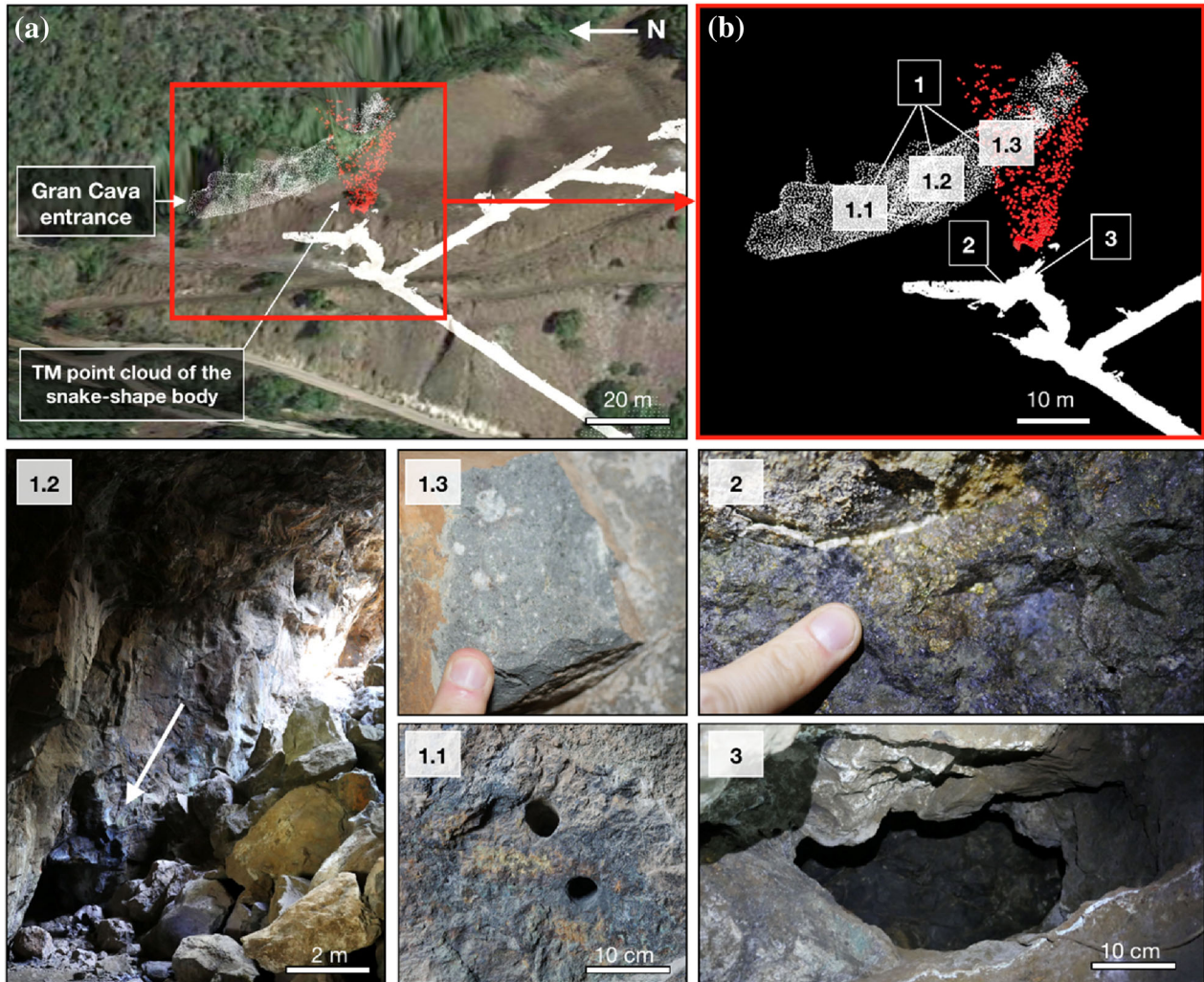
Figure 7. In situ survey photographs and point cloud data visualization at the Temperino mine: (**a**) 3D visualization of the Gran Cava and tunnels TLS surveys (white point clouds) together with the red point cloud that has been created using the TM acquired data to locate the snake-shape body; (**b**) in situ geological survey points and photographs taken inside the Gran Cava area and underground to verify the presence of the reconstructed mafic porphyry (PM) and the related Cu-Fe mineralization. In particular, photographs 1.1–1.2 (white arrow) and 1.3 show outcrops of PM inside the large Gran Cava cavity to small tunnels that were carved near the upper part of the reconstructed snake-shape body. Photographs 2 and 3 show the presence of Cu–Fe-bearing ore (the presence of chalcopyrite ($CuFeS_2$) was well observed) and several little tunnels carved all around the reconstructed snake-shape body relatively.

density polar map in Fig. 5f). A unique georeferenced 3D environment was then developed to carry out the interpretation of the TM data taking into account all the acquired data.

The Leapfrog Geo Seequent software (Seequent Software, 2022) and the CloudCompare (CC) open-source software (CloudCompare, 2022) were used for point cloud data management, visualization and analysis. Using the whole of the available geological data (TLS point cloud data, TM back-projection point cloud data and the 3D geological model) led to a more reliable interpretation of the TM data. Several structures were observed within the acceptance of the MIMA detector and thanks to the created 3D geological model, the in situ surveys (Fig. 7) and the knowledge on the geological history, it was possible to correlate the density differences shown in Figure 5f with the surveyed geological units as well as to validate the TM measurement.

Some of the very low-density zones are both unknown and known cavities (such as the Gran Cava); other intermediate density values are where

the marble host rocks (MAS) and felsic porphyry dike (PFC) lie embedded, as confirmed by the underground/on-the-surface geological surveys (Fig. 6), while the high-density zone is a potential Cu–Fe ore body. The latter was the object that the MIMA detector was looking for, i.e., possible high-density ore body of mining interest. This "snake-shape" body is characterized by a well-defined NNW–SSE orientation and a sub-vertical geometry (Fig. 5f), which is consistent with the general setting of the emplaced metasomatic (skarn) and igneous bodies (mafic porphyry) exploited in the past in the Temperino mining area (Da Mommio et al., 2010; Vezzoni, 2014). As reported by Vezzoni (2014), the mafic porphyry bodies (PM) have stronger variations in orientation (from N–S to E–W) and extension (unit of meters), which are different from the acid one (PFC) that are elongated NW–SE at the center of the skarn body for hundreds of meters with thickness of 5–10 m. By correlating these features together with the TM data, it was possible to observe that the "snake-shape" body had a thickness of about 2–4 m, with relative average density values along the LoS, ranging from 3.0 to 3.4 g/cm^3. It is in contact with lower density host rocks of about 2.5–2.9 g/cm^3 (Fig. 5f) and can be interpreted as a mafic porphyry intrusion associated with the relative metamorphic contact rocks generated through interactions with the host skarn body (Fig. 8). The Cu–Fe ores have overprinted the skarn rocks at the contact with the mafic porphyry intrusions and dikes with mineral assemblages dominated by chalcopyrite, pyrite and pyrrhotite (see density values in Table 1). Obviously, the TM technique returns average density values along the various LoS of the detector (Fig. 8), and so these density values often underestimate the higher density value present along each LoS. Indeed, the average density of each LoS depends on the complexity of the geological structures relations; the more complex is the geological setting, the noisier and more unclear the TM transmission and density maps become.
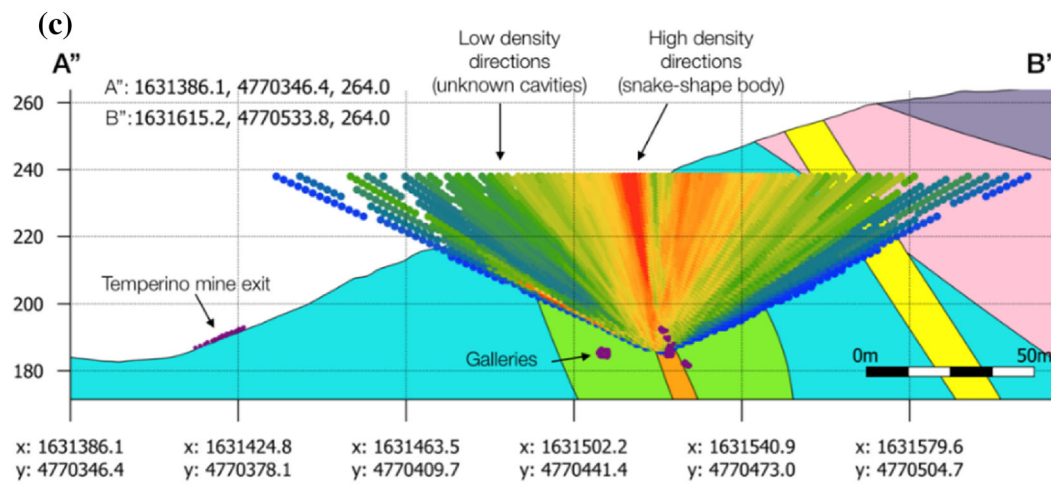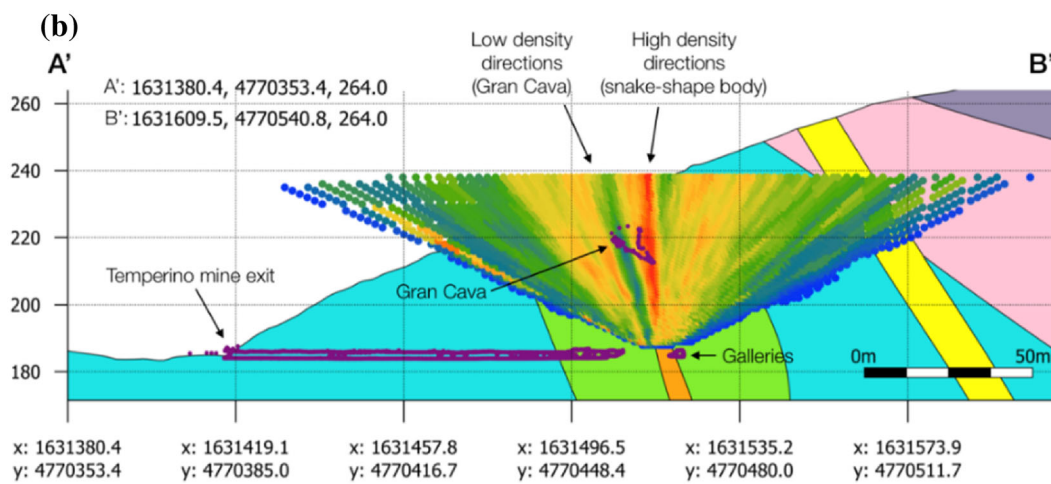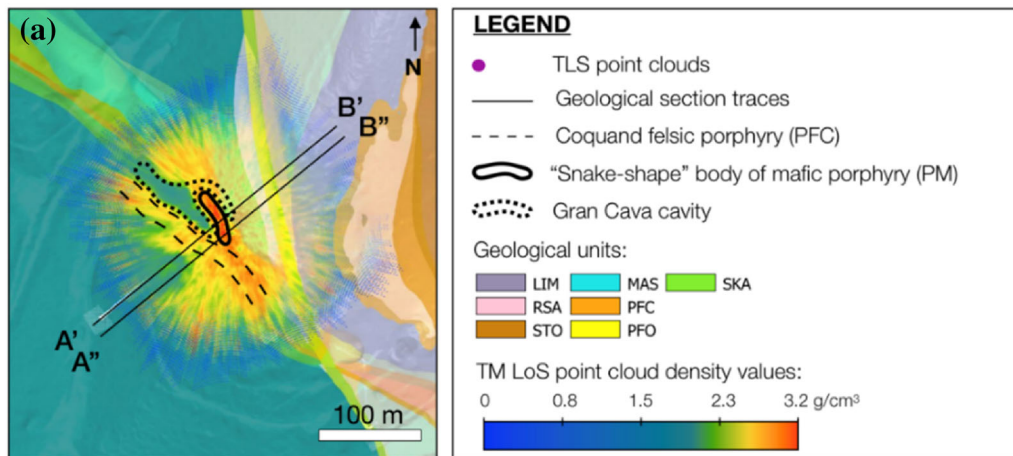
At the Temperino mine, the skarn mining exploitation was often driven by the presence of these mafic porphyry intrusions because economically useful minerals, enriched in Cu–Fe–Pb–Zn, are associated with them. In fact, the data show that some existing cavities (Figs. 7a, 8, 9) have been excavated close to the "snake–shape" body where the Cu–Fe–Pb–Zn ores were exploited.

To validate these observations, we calculated the identified high-density vein locations in the 3D model by applying the back-projection method to the TM data (Bonechi et al., 2015, 2019; Borselli et al., 2022). This method allowed us to create a 3D point cloud of the "base" and "vault" of the high-density body with average accuracy of about 0.5–1 m (Fig. 9). An in situ inspection inside the Gran Cava and the adjacent small tunnels confirmed the upper part of the identified mafic porphyry intrusion outcrops, the snake-shape body outcrops (Fig. 7). Also, the presence of a Cu–Fe-bearing ore (primarily chalcopyrite) at the bottom of the snake-shape body inside the Temperino mine, nearby the MIMA detector, points to a potential ore body (Fig. 9).

DISCUSSION

In the last two decades, muography has been applied to a wide range of research fields and in several multidisciplinary projects with promising results mainly for volcanological applications (Tanaka et al., 2007; Saracino & Cârloganu, 2012; D'Alessandro et al., 2019; Tioukov et al., 2019) but also in the field of mining exploration (Schouten & Ledru, 2018; Schouten, 2019). For the latter, muography has the advantage that, with a passive, non-invasive method, 2D/3D mine density maps can be obtained at relative low cost with respect to other direct methods (e.g., drilling). Moreover, a higher accuracy (meters/tens of meters) depending on the dimensions of the studied target and on the target-detector distance, may be achieved with respect to the other available geophysical methods (Kaiser, 2019;). There are also disadvantages in the method, mainly due to logistics related to the safe transport and installation of the used detector, and to the lengthy data acquisition period (from days to months) that directly depend on underground depth, on tracker altazimuthal configuration and on crossed matter within the studied target (Bonechi et al., 2020a, 2020b). Moreover, the reliability of the simulations output used to obtain the relative transmission and average density along the LoS depends on the complexity of the studied geological setting and on the ancillary data of the studied area, e.g., resolution and extension of available DTM and geological information. It follows that, to achieve a reliable interpretation of the muon imaging results, it may be useful to have the most detailed DTM possible and a preliminary geological model (which, if not available, could be created) that could give some advice to the interpretation phase. To this day,

(a)

LEGEND

• TLS point clouds
— Geological section traces
- - - Coquand felsic porphyry (PFC)
⬭ "Snake-shape" body of mafic porphyry (PM)
⬭ Gran Cava cavity

Geological units:
LIM   MAS   SKA
RSA   PFC
STO   PFO

TM LoS point cloud density values:
0   0.8   1.5   2.3   3.2 g/cm³

(b)

A': 1631380.4, 4770353.4, 264.0
B': 1631609.5, 4770540.8, 264.0

Low density directions (Gran Cava)
High density directions (snake-shape body)

Gran Cava

Temperino mine exit

Galleries

0m   50m

| x: 1631380.4 | x: 1631419.1 | x: 1631457.8 | x: 1631496.5 | x: 1631535.2 | x: 1631573.9 |
| y: 4770353.4 | y: 4770385.0 | y: 4770416.7 | y: 4770448.4 | y: 4770480.0 | y: 4770511.7 |

(c)

A": 1631386.1, 4770346.4, 264.0
B": 1631615.2, 4770533.8, 264.0

Low density directions (unknown cavities)
High density directions (snake-shape body)

Temperino mine exit

Galleries

0m   50m

| x: 1631386.1 | x: 1631424.8 | x: 1631463.5 | x: 1631502.2 | x: 1631540.9 | x: 1631579.6 |
| y: 4770346.4 | y: 4770378.1 | y: 4770409.7 | y: 4770441.4 | y: 4770473.0 | y: 4770504.7 |

◄**Figure 8.** TM point cloud density data visualization. (**a**) Orthogonal view of the LoS $\bar{\rho}(\theta, \varphi)$ values from muon imaging data together with the geological map and the two section traces A'B' and A"B". The geological interpretation process allowed us to recognize the geometry of a mafic porphyry dike PM (the snake-shape body), the Coquand felsic porphyry dike PFC and unknown and known cavities. It is noteworthy that the Gran Cava cavities developed around the "snake-shape" body for mining exploitation. In the two sections, the whole available data are reported to spatially understand the relationship between the point cloud density values obtained using the TM technique and the TLS survey and geology. (**b**) Section A'B' shows these 3D-like shapes because it does not across the center of MIMA detector. (**c**) Section A"B", crossing the center of MIMA, shows a clearer directional $\bar{\rho}(\theta, \varphi)$.

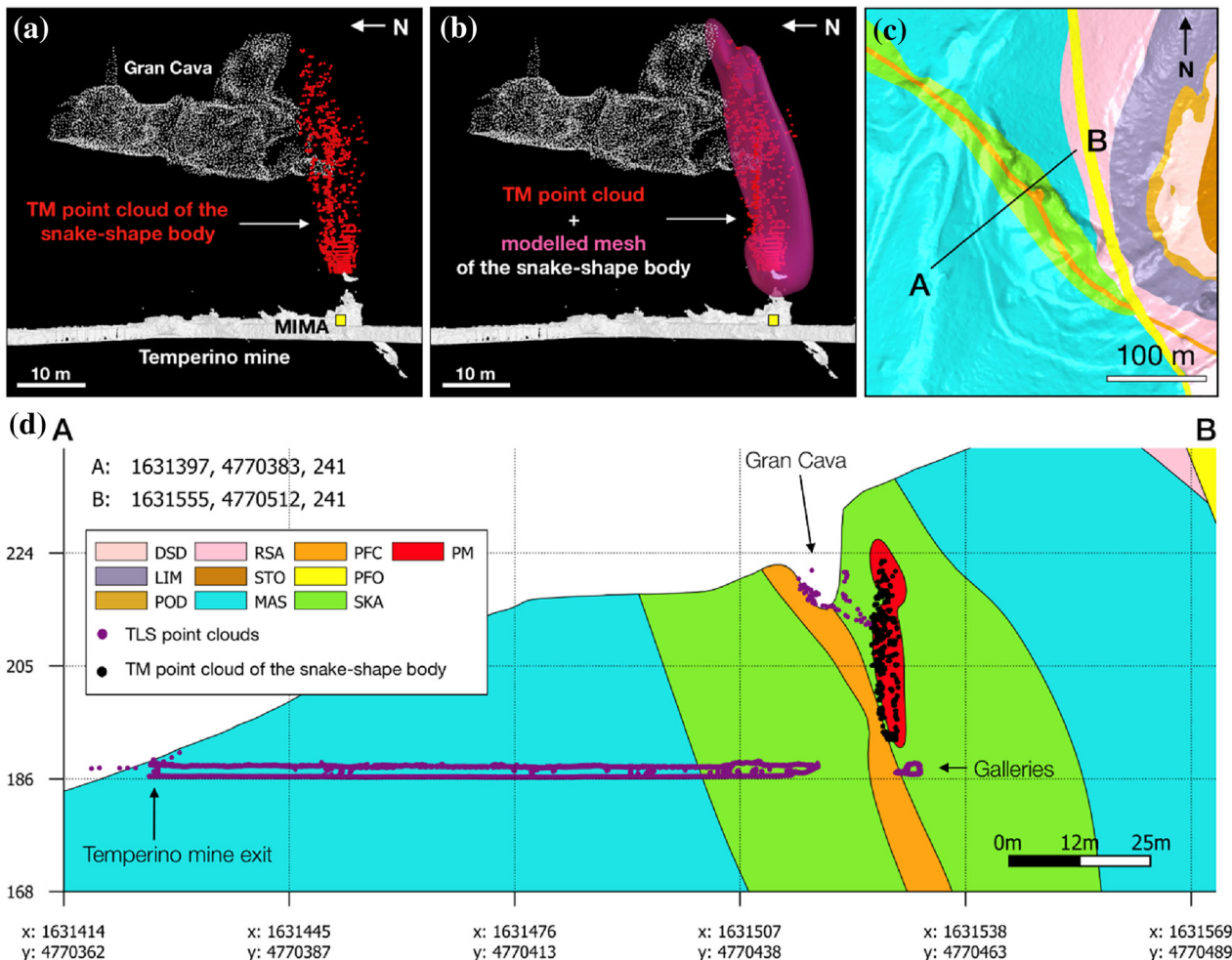the great challenge in the muon imaging process is being able to really understand what the 2D transmission and average density maps and the 3D point clouds density data show and how reliable they are. In fact, the appearance of the transmission maps depends on the geometry of the used detector (shape and dimensions of the detection surface), the studied target and the surrounding environment (materials properties and thicknesses). Also, some errors could be introduced by muon physics related issues, during the acquisition and analysis steps. Indeed, it is known that, during the free-sky configuration measurement, the obtained data could be characterized by a non-muon background noise different from the underground one, and that the muon flux can change during the acquisition time as a result of seasonal cycles and solar variations, especially for low energy muons. Also, in the presented study, we had to deal with these potential

Figure 9. TM point cloud data modeling and visualization. (**a**) 3D view of the reconstructed "snake-shape" ore body from TM imaging applying the back-projection algorithm. (**b**) The same view of (**a**) with addition of a mesh modeled on the snake-shape body point cloud. (**c**) Geological map with geological section AB shown in (**d**). In the section (**d**) is shown the identified high-density vein modeled on the TM point cloud data acquired with the MIMA detector inside the skarn body at the Temperino mine.

errors, but it was pointed out that the effect of the solar modulation on the muon flux at the Temperino latitude was relatively smaller than the statistical errors typical of our measurements. It also resulted in underestimation or overestimation of all measured densities and thus had no significant effect on their relative comparison.

Moreover, systematics errors rising from the ratio between the underground and free-sky measurements, due to the changing of muons spectrum with depth, could affect the output. The evaluation and quantification of these kind of potential errors (usually considered negligible) is one of the main topics we are dealing with to quantify correctly uncertainties related with muon imaging results. Among the future challenges for the presented case study, we will deepen the understanding of how the outcomes of the muon imaging technique could change using different available muon flux dataset instead of the ADAMO one.

For the purpose of this study, i.e., muography applied for mining activities, it was fundamental to have as clear knowledge as possible of the geometries and densities of the rock distributions in the area to correctly take advantage of TM data and to verify the method. However, although the presented workflow needs improvement, the results of this study highlighted the potential of TM muon imaging as a complementary geophysical method to the other ones already employed in mineral ore prospecting and mining activities.

CONCLUSIONS

Transmission-based muography was used to image an inner part of the Cu–Fe–Zn–Pb(–Ag) sulfide skarn body at the Temperino mine (Campiglia Marittima, Italy) in the San Silvestro Archaeological and Mining Park. This work represents one of the first examples of a muon radiography application for skarn ore bodies prospecting in the field of mining exploration. To achieve this goal, it was essential to combine in-depth geological knowledge of the area together the physics results from muography. The obtained results highlight the potential of muon radiography for mining activities. This study has allowed to:

(a)   verify the reliability of TM for the visualization of the inner structures, belonging to the rock bodies overlying the muon detector;

(b)   validate muography as a support tool for other mining exploration methods, to visualize underground rock density differences distributions, to indicate the presence of potential ore bodies (or cavities), and to give indications for the directions of future excavations or drilling;

(c)   demonstrate that even one TM measurement can give useful information about ore deposits; and

(d)   demonstrate the usefulness of 3D management of muographic data in interpreting the results together with 3D geological modeling.

The workflow presented in this paper is applicable to all cases where a mine gallery already exists. In the future, further measurements will be performed in other locations of the Temperino mine with the aim of implementing the simulations environment for a more complex geological setting. The same workflow will be tested using additional muon flux datasets from literature for further validation of the used one, i.e., ADAMO. In conclusion, the main future goals of this research concern the speeding up of the muographic data analysis and processing, the understanding of the influence that field surveys and topographical data play on the created 2D/3D muographic results in terms of accuracy.

DECLARATIONS

Conflict of Interest   The authors declare that they have no known competing financial interests or personal relationships that could have appeared to influence the work reported in this paper.

OPEN ACCESS

REFERENCES

Acocella, V., Rossetti, F., Faccenna, C., Funiciello, R., & Lazzarotto, A. (2000). Strike-slip faulting and pluton emplacement in Southern Tuscany: The Campiglia case. *Bollettino. Societa Geologica Italiana, 119*, 517–528.

Alvarez, L. W., Anderson, J. A., Bedwei, F. E., Burkhard, J., Fakhry, A., Girgis, A., Goneid, A., Hassan, F., Iverson, D., Lynch, G., Miligy, Z., Moussa, A. H., Sharkawi, M., & Yazolino, L. (1970). Search for Hidden Chambers in the Pyramids: The structure of the Second Pyramid of Giza is determined by cosmic-ray absorption. *Science, 167*(3919), 832–839.

Baccani, G., Bonechi, L., Ciaranfi, R., Cimmino, L., Ciulli, V., D'Alessandro, R., Melon, B., Noli, P., Saracino, G., & Viliani, L. (2018). *The MIMA project. Design, construction and performances of a compact hodoscope for muon radiography applications in the context of Archaeology and geophysical prospections.* https://doi.org/10.48550/ARXIV.1806.11398.

Baccani, G., Bonechi, L., Bongi, M., Brocchini, D., Casagli, N., Ciaranfi, R., Cimmino, L., Ciulli, V., D'Alessandro, R., Del Ventisette, C., Dini, A., Gigli, G., Gonzi, S., Guideri, S., Lombardi, L., Melon, B., Mori, N., Nocentini, M., Noli, P., … Viliani, L. (2019). Muon radiography of ancient mines: The San Silvestro Archaeo-Mining Park (Campiglia Marittima, Tuscany). *Universe, 5*(1), 34.

Baccani, G., Bonechi, L., Bongi, M., Casagli, N., Ciaranfi, R., Ciulli, V., D'Alessandro, R., Gonzi, S., Lombardi, L., Morelli, S., Nocentini, M., Pazzi, V., Tacconi Stefanelli, C., & Viliani, L. (2021). The reliability of muography applied in the detection of the animal burrows within River Levees validated by means of geophysical techniques. *Journal of Applied Geophysics, 191*, 104376.

Bonechi, L., Bongi, M., Fedele, D., Grandi, M., Ricciarini, S. B., & Vannuccini, E. (2005). Development of the ADAMO detector: Test with cosmic rays at different zenith angles. *29th International Cosmic Ray Conference (Pune), 9*, 283–286.

Bonechi, L., Ambrosino, F., Cimmino, L., D'Alessandro, R., Macedonio, G., Melon, B., Mori, N., Noli, P., Saracino, G., Strolin, P., Giudicepietro, F., Martini, M., Orazi, M., & Peluso, R. (2018). The MURAVES project and other parallel activities on muon absorption radiography. *EPJ Web of Conferences, 182*, 02015. https://doi.org/10.1051/epjconf/201818202015.

Bonechi, L., Baccani, G., Bongi, M., Brocchini, D., Casagli, N., Ciaranfi, R., Cimmino, L., Ciulli, V., D'Alessandro, R., Del Ventisette, C., Dini, A., Gigli, G., Gonzi, S., Guideri, S., Lombardi, L., Melon, B., Mori, N., Nocentini, M., Noli, P., & Viliani, L. (2019). Tests of a novel imaging algorithm to localize hidden objects or cavities with muon radiography. *Philosophical Transactions of the Royal Society A: Mathematical, Physical and Engineering Sciences, 377*(2137), 20180063.

Bonechi, L., Baccani, G., Bongi, M., Brocchini, D., Casagli, N., Ciaranfi, R., Cimmino, L., Ciulli, V., D'Alessandro, R., Ventisette, C. D., D'Errico, M., Dini, A., Gigli, G., Gonzi, S., Guideri, S., Lombardi, L., Mori, N., Nocentini, M., Starodubtsev, O., … Viliani, L. (2020a). Multidisciplinary applications of muon radiography using the MIMA detector. *Journal of Instrumentation, 15*(05), C05030–C05030.

Bonechi, L., D'Alessandro, R., & Giammanco, A. (2020b). Atmospheric muons as an imaging tool. *Reviews in Physics, 5*, 100038.

Bonechi, L., D'Alessandro, R., Mori, N., & Viliani, L. (2015). A projective reconstruction method of underground or hidden structures using atmospheric muon absorption data. *Journal of Instrumentation, 10*(02), P02003–P02003.

Bonomi, G., Donzella, A., Pagano, D., Zenoni, A., Zumerle, G., & Zurlo, N. (2022). A Monte Carlo muon generator for cosmic-ray muon applications. *Journal for Advanced Instrumentation in Science.* https://doi.org/10.31526/JAIS.2022.290.

Borselli, D. (2018). *Muographic study of the Temperino mine with the MIMA detector: Development and test of an algorithm for identification and reconstruction of cavities in three dimensions [Master's degree thesis in Physical and Astrophysical Sciences].* University of Florence.

Borselli, D., Beni, T., Bonechi, L., Bongi, M., Brocchini, D., Casagli, N., Ciaranfi, R., Cimmino, L., Ciulli, V., D'Alessandro, R., Dini, A., Frosin, C., Gigli, G., Gonzi, S., Guideri, S., Lombardi, L., Nocentini, M., & Saracino, G. (2022). Three-dimensional muon imaging of cavities inside the Temperino mine (Italy). *Scientific Reports, 12*(1), 22329.

Borsi, S., Ferrara, G., & Tongiorgi, E. (1967). Determinazione con il metodo K/Ar delle età delle rocce magmatiche della Toscana. *Bollettino Societa Geologica Italiana, 86*, 403–410.

Brocchini, D., Deravignone, L., & Dellavalle, G. (2017). Unveil the traces of ancient mining. *Acta Geoturistica, 8*(1), 11–19.

Bryman, D., Bueno, J., Davis, K., Kaminski, V., Liu, Z., Oldenburg, D., Pilkington, M., & Sawyer, R. (2014). Muon Geotomography—Bringing New Physics to Orebody Imaging. In K. D. Kelley & H. C. Golden, *Building Exploration Capability for the 21st Century*. Society of Economic Geologists. https://doi.org/10.5382/SP.18.11.

Carbone, D., Gibert, D., Marteau, J., Diament, M., Zuccarello, L., & Galichet, E. (2014). An experiment of muon radiography at Mt Etna (Italy). *Geophysical Journal International, 196*(2), 633–643.

Cimmino, L., Ambrosino, F., Bonechi, L., Ciaranfi, R., D'Alessandro, R., Masone, V., Mori, N., Noli, P., Saracino, G., & Strolin, P. (2017). The MURAVES telescope front-end electronics and data acquisition. *Annals of Geophysics, 60*(1), 4.

CloudCompare. (2022). *CloudCompare.* https://www.danielgm.net/cc/.

D'Alessandro, R., Ambrosino, F., Baccani, G., Bonechi, L., Bongi, M., Caputo, A., Ciaranfi, R., Cimmino, L., Ciulli, V., D'Errico, M., Giudicepietro, F., Gonzi, S., Macedonio, G., Masone, V., Melon, B., Mori, N., Noli, P., Orazi, M., Passeggio, P., … Viliani, L. (2019). Volcanoes in Italy and the role of muon radiography. *Philosophical Transactions of the Royal Society A: Mathematical, Physical and Engineering Sciences, 377*(2137), 20180050.

Da Mommio, A., Iaccarino, S., Vezzoni, S., Dini, A., Rocchi, S., Brocchini, D., Guideri, S., & Sbrilli, L. (2010). Valorizzazione del geosito «Sezione Coquand», miniera del Temperino (Parco Archeominerario di San Silvestro, Campiglia Marittima). *Atti della Società Toscana di Scienze Naturali Residente in Pisa Memorie serie A, 115*, 55–72.

Dini, A., Gianelli, G., Puxeddu, M., & Ruggieri, G. (2005). Origin and evolution of Pliocene-Pleistocene granites from the Larderello geothermal field (Tuscan Magmatic Province, Italy). *Lithos, 81*(1–4), 1–31.

Dini, A., Orlandi, P., & Vezzoni, S. (2013). Temperino e Lanzi. Le paragenesi primarie dello skarn. *Rivista Mineralogica Italiana, 1*, 28–39.

Edward Pelham, G. (1955). Cosmic rays measure overburden of tunnel. *Commonwealth Engineer*, 455–457.

Gonzi, S., Ambrosino, F., Andreetto, P., Bonechi, L., Bonomi, G., Borselli, D., Bottai, S., Buhles, T., Calliari, I., Checchia, P., Chiarotti, U., Cialdai, C., Ciaranfi, R., Cimmino, L., Ciulli, V., D'Alessandro, M., D'Errico, M., Finke, F., Franzen, A., … Volzone, F. (2022). Imaging of the Inner Zone of Blast Furnaces Using MuonRadiography: The BLEMAB Project. *Journal for Advanced Instrumentation in Science*. https://doi.org/10.31526/JAIS.2022.272.

Grieder, P. K. F. (2001). *Cosmic rays at Earth: Researcher's reference manual and data book* (1st ed.). Elsevier.

Groom, D. E., Mokhov, N. V., & Striganov, S. I. (2001). Muon Stopping Power and Range Tables 10 MeV–100 TeV. *Atomic Data and Nuclear Data Tables, 78*(2), 183–356.

Guardincerri, E., Rowe, C., Schultz-Fellenz, E., Roy, M., George, N., Morris, C., Bacon, J., Durham, M., Morley, D., Plaud-Ramos, K., Poulson, D., Baker, D., Bonneville, A., & Kouzes, R. (2017). 3D cosmic ray muon tomography from an underground tunnel. *Pure and Applied Geophysics, 174*(5), 2133–2141.

Jourde, K., Gibert, D., Marteau, J., de Bremond d'Ars, J., & Komorowski, J.-C. (2016). Muon dynamic radiography of density changes induced by hydrothermal activity at the La Soufrière of Guadeloupe volcano. *Scientific Reports, 6*(1), 33406.

Kaiser, R. (2019). Muography: Overview and future directions. *Philosophical Transactions of the Royal Society A: Mathematical, Physical and Engineering Sciences, 377*(2137), 20180049.

Lechmann, A., Mair, D., Ariga, A., Ariga, T., Ereditato, A., Nishiyama, R., Pistillo, C., Scampoli, P., Schlunegger, F., & Vladymyrov, M. (2018). The effect of rock composition on muon tomography measurements. *Solid Earth, 9*(6), 1517–1533.

Lesparre, N., Gibert, D., Marteau, J., Komorowski, J.-C., Nicollin, F., & Coutant, O. (2012). Density muon radiography of La Soufrière of Guadeloupe volcano: Comparison with geological, electrical resistivity and gravity data. *Geophysical Journal International, 190*(2), 1008–1019.

Lin, J.-W., Chen, Y.-F., Sheu, R.-J., & Jiang, S.-H. (2010). Measurement of angular distribution of cosmic-ray muon fluence rate. *Nuclear Instruments and Methods in Physics Research Section A: Accelerators, Spectrometers, Detectors and Associated Equipment, 619*(1–3), 24–27.

Mahon, D., Clarkson, A., Gardner, S., Ireland, D., Jebali, R., Kaiser, R., Ryan, M., Shearer, C., & Yang, G. (2019). First-of-a-kind muography for nuclear waste characterization. *Philosophical Transactions of the Royal Society A: Mathematical, Physical and Engineering Sciences, 377*(2137), 20180048.

Malmqvist, L., Jönsson, G., Kristiansson, K., & Jacobsson, L. (1979). Theoretical studies of in-situ rock density determinations using underground cosmic-ray muon intensity measurements with application in mining geophysics. *Geophysics, 44*(9), 1549–1569.

Meinert, L. D., Dipple, G. M., & Nicolescu, S. (2005). World Skarn Deposits. In J. W. Hedenquist, J. F. H. Thompson, R. J. Goldfarb, & J. P. Richards, *One Hundredth Anniversary Volume*. Society of Economic Geologists. https://doi.org/10.5382/AV100.11.

Menichelli, M., Ansoldi, S., Bari, M., Basset, M., Battiston, R., Blasko, S., Coren, F., Fiori, E., Giannini, G., Iugovaz, D., Papi, A., Reia, S., & Scian, G. (2007). A scintillating fibres tracker detector for archaeological applications. *Nuclear Instruments and Methods in Physics Research Section A: Accelerators, Spectrometers, Detectors and Associated Equipment, 572*(1), 262–265.

Okada, K. (2021). A historical overview of the past three decades of mineral exploration technology. *Natural Resources Research, 30*(4), 2839–2860.

Olive, K. A. (2016). Review of particle physics. *Chinese Physics C, 40*(10), 100001.

Paoli, G., Dini, A., & Rocchi, S. (2019). Footprints of element mobility during metasomatism linked to a late Miocene peraluminous granite intruding a carbonate host (Campiglia Marittima, Tuscany). *International Journal of Earth Sciences, 108*(5), 1617–1641.

Procureur, S. (2018). Muon imaging: Principles, technologies and applications. *Nuclear Instruments and Methods in Physics Research Section A: Accelerators, Spectrometers, Detectors and Associated Equipment, 878*, 169–179.

Saracino, G., Ambrosino, F., Bonechi, L., Cimmino, L., D'Alessandro, R., D'Errico, M., Noli, P., Scognamiglio, L., & Strolin, P. (2019). Applications of muon absorption radiography to the fields of archaeology and civil engineering. *Philosophical Transactions of the Royal Society A: Mathematical, Physical and Engineering Sciences, 377*(2137), 20180057.

Saracino, G., & Cârloganu, C. (2012). Looking at volcanoes with cosmic-ray muons. *Physics Today, 65*(12), 60–61.

Schouten, D. (2019). Muon geotomography: Selected case studies. *Philosophical Transactions of the Royal Society A: Mathematical, Physical and Engineering Sciences, 377*(2137), 20180061.

Schouten, D., & Ledru, P. (2018). Muon Tomography Applied to a Dense Uranium Deposit at the McArthur River Mine. *Journal of Geophysical Research: Solid Earth, 123*(10), 8637–8652.

Sciarra, A., Benvenuti, M., Boschi, C., Dini, A., Ruggieri, G., & Arias, A. (2015). Geothermal resources, ore deposits and carbon mineral sequestration in hydrothermal areas of Southern Tuscany. *Geological Field Trips, 7*(1.2), 1–91.

Seequent Software (2022). Leapfrog Geo software version 2021.2. https://www.seequent.com/products-solutions/leapfrog-geo/?gclid=CjwKCAjw4ayUBhA4EiwATWyBrq8hIUs5EKTacYt1CsfZHq15BqQzVZ4k1-_RtEe9VEAR1padPJLcjBoC4f0QAvD_BwE.

Tanaka, H. (2017). Muography. *Proceedings of The 3rd International Symposium on "Quest for the Origin of Particles and the Universe"—PoS(KMI2017)*, 026. https://doi.org/10.22323/1.294.0026.

Tanaka, H. K. M. (2015). Muographic mapping of the subsurface density structures in Miura, Boso and Izu peninsulas. *Japan. Scientific Reports, 5*(1), 8305.

Tanaka, H. K. M. (2016). Instant snapshot of the internal structure of Unzen lava dome, Japan with airborne muography. *Scientific Reports, 6*(1), 39741.

Tanaka, H. K. M., Kusagaya, T., & Shinohara, H. (2014). Radiographic visualization of magma dynamics in an erupting volcano. *Nature Communications, 5*(1), 3381.

Tanaka, H., Nakano, T., Takahashi, S., Yoshida, J., Takeo, M., Oikawa, J., Ohminato, T., Aoki, Y., Koyama, E., & Tsuji, H. (2007). High resolution imaging in the inhomogeneous crust with cosmic-ray muon radiography: The density structure

below the volcanic crater floor of Mt. Asama, Japan. *Earth and Planetary Science Letters, 263*(1–2), 104–113..

Tanaka, H. K. M., & Oláh, L. (2019). Overview of muographers. *Philosophical Transactions of the Royal Society A: Mathematical, Physical and Engineering Sciences, 377*(2137), 20180143.

Tinagli, L., Paoli, G., & Vezzoni, S. (2021). Snake-shaped carbonate folds replaced by skarn (Campiglia Marittima, Italy). *International Journal of Earth Sciences, 110*(1), 113–114.

Tioukov, V., Alexandrov, A., Bozza, C., Consiglio, L., D'Ambrosio, N., De Lellis, G., De Sio, C., Giudicepietro, F., Macedonio, G., Miyamoto, S., Nishiyama, R., Orazi, M., Peluso, R., Sheshukov, A., Sirignano, C., Stellacci, S. M., Strolin, P., & Tanaka, H. K. M. (2019). First muography of Stromboli volcano. *Scientific Reports, 9*(1), 6695.

Tioukov, V., De Lellis, G., Strolin, P., Consiglio, L., Sheshukov, A., Orazi, M., Peluso, R., Bozza, C., De Sio, C., Stellacci, S. M., Sirignano, C., D'Ambrosio, N., Miyamoto, S., Nishiyama, R., & Tanaka, H. (2017). Muography with nuclear emulsions—Stromboli and other projects. *Annals of Geophysics, 60*(1), 10.

Regione Toscana. (2022). [Geoscopio Webgis]. https://www.regione.toscana.it/-/geoscopio-wms.

Vanini, S., Calvini, P., Checchia, P., Rigoni Garola, A., Klinger, J., Zumerle, G., Bonomi, G., Donzella, A., & Zenoni, A. (2019). Muography of different structures using muon scattering and absorption algorithms. *Philosophical Transactions of the Royal Society A: Mathematical, Physical and Engineering Sciences, 377*(2137), 20180051.

Vezzoni, S. (2014). *Evolution of a pluton-porphyry-skarn system: The Temperino-Lanzi mine (Campiglia Marittima, Tuscany)* [PhD Thesis, Università di Pisa]. Sistema bibliotecario di ateneo.

Vezzoni, S., Dini, A., & Rocchi, S. (2016). Reverse telescoping in a distal skarn system (Campiglia Marittima, Italy). *Ore Geology Reviews, 77*, 176–193.

Vezzoni, S., Rocchi, S., & Dini, A. (2018). Lateral extrusion of a thermally weakened pluton overburden (Campiglia Marittima, Tuscany). *International Journal of Earth Sciences, 107*(4), 1343–1355.

Yang, T., Gao, J., Gu, Z., Dagva, B., & Tserenpil, B. (2013). Petrophysical properties (density and magnetization) of rocks from the Suhbaatar-Ulaanbaatar-Dalandzadgad geophysical profile in Mongolia and their implications. *The Scientific World Journal, 2013*, 1–12.

Zhang, Z.-X., Enqvist, T., Holma, M., & Kuusiniemi, P. (2020). Muography and Its Potential Applications to Mining and Rock Engineering. *Rock Mechanics and Rock Engineering, 53*(11), 4893–4907.

Zyla, P. A., Barnett, R. M., Beringer, J., Dahl, O., Dwyer, D. A., Groom, D. E., Lin, C.-J., Lugovsky, K. S., Pianori, E., Robinson, D. J., Wohl, C. G., Yao, W.-M., Agashe, K., Aielli, G., Allanach, B. C., Amsler, C., Antonelli, M., Aschenauer, E. C., Asner, D. M., … Zheng, W. (2020). Review of particle physics. *Progress of Theoretical and Experimental Physics, 2020*(8), 083C01.